

**REDUCED-ORDER MODEL AND NEURAL OPERATORS FOR
STOCHASTIC MECHANICS PROBLEMS UNDER
PARAMETRIC UNCERTAINTY**

NAVANEETH N



DEPARTMENT OF APPLIED MECHANICS

INDIAN INSTITUTE OF TECHNOLOGY DELHI

SEPTEMBER 2025

© Indian Institute of Technology Delhi (IITD), New Delhi, 2025

**REDUCED-ORDER MODEL AND NEURAL OPERATORS FOR
STOCHASTIC MECHANICS PROBLEMS UNDER
PARAMETRIC UNCERTAINTY**

by

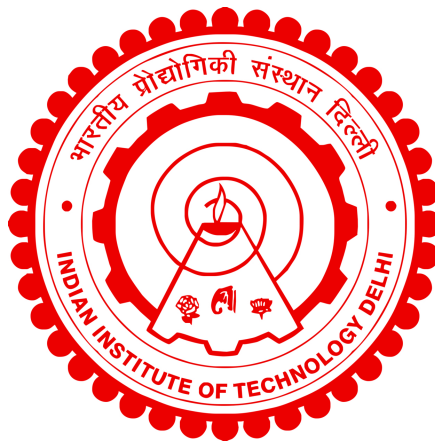
NAVANEETH N

Department of Applied Mechancics

Submitted

in partial fulfillment of the requirements of the degree of Doctor of Philosophy

to the



INDIAN INSTITUTE OF TECHNOLOGY DELHI

SEPTEMBER 2025

Certificate

This is to certify that the thesis titled **Reduced-Order Model and Neural Operators for Stochastic Mechanics Problems Under Parametric Uncertainty**, submitted by **Mr. Navaneeth**, to the Indian Institute of Technology, Delhi, for the award of the degree of **Doctor of Philosophy**, is a bonafide record of the research work done by him under our supervision and guidance. The contents of this thesis, in full or in parts, have not been submitted to any other Institute or University for the award of any degree or diploma.

Date: 24-09-2025

Place: New Delhi

Dr. Souvik Chakraborty
Department of Applied Mechanics,
Indian Institute of Technology Delhi.
IIT Delhi, 110016

Acknowledgement

This thesis represents the culmination of my relentless efforts toward the successful completion of my Ph.D. journey. Beyond the attainment of an academic degree, this endeavor has been a transformative experience that has profoundly molded me as an individual. This accomplishment would not have been possible without the support and encouragement of numerous people. Even though words are too feeble to convey my gratitude, I avail myself of this opportunity to express my heartfelt thanks.

First and foremost, I would like to extend my deepest gratitude to my research supervisor, Prof. Souvik Chakraborty, for his unstinting backing, meticulous guidance, and encouragement throughout the pursuit of my research. The enlightening discussions, keen supervision, and uncompromising standards he maintained were instrumental in shaping my research. The freedom and constructive feedback he provided greatly enhanced my understanding and progress, making my academic tenure at IIT Delhi both productive and fulfilling. Furthermore, his initiative was pivotal in enabling me to secure the prestigious Prime Ministers Research Fellowship (PMRF), which significantly facilitated my research journey.

I am profoundly thankful to the Department of Applied Mechanics at IIT Delhi for its unconditional support. The Department's commitment to fostering interdisciplinary and innovative research sets it apart, creating a conducive condition for academic enterprise. My heartfelt thanks go to Prof. Santosh Kapuria, Head of the Department, and Prof. B. P. Patel, Chair of the Departmental Research Committee, for their encouragement and guidance during my Ph.D.

I extend my sincere gratitude to my research committee members Prof. Ajeet Kumar, for chairing the committee, Prof. Sitikanta Roy, and Prof. Vasant Matsagar, for serving as internal and external experts and for their constructive feedback. I also thank Prof. Saikat Sarkar for the insightful discussions that significantly enriched my research. My sincere appreciation goes to all the faculty members of the department for their guidance and the conversations that provided the intellectual impetus. I am particularly thankful to the directors of IIT Delhi, Prof. V. Ramgopal Rao and Prof. Rangan Banerjee, for the research-friendly atmosphere and for providing seamless facilities, especially during the uncertain times of the pandemic.

I would like to extend my deep gratitude to the government of India for having conferred upon me the prestigious Prime Ministers Research Fellowship (PMRF), which proved to be a crucial financial succor to me during my doctoral tenure. The annual reviews conducted under the PMRF program offered valuable feedback that bolstered my research. Additionally, the opportunities furnished by PMRF to interact with students outside the institute and attend international conferences were salutary experiences. A notable highlight was the fellowship-supported visit to Greece, which allowed me to engage with experts in my fieldan experience I will always cherish.

Collaboration has been a cornerstone of my research, and my gratitude due also to my co-authors and collaborators. Working with Prof. Sondipon Adhikari, fellow M.Tech researchers Aarya and Rakesh Kumar, as well as Rohan Thorat and Dr. Rajdip Nayek, was a rewarding and fruitful experience. Their contributions and insights significantly enhanced the quality of my work. I am deeply indebted to my lab mates and friends for their unwavering support and companionship, which made my research term at IIT Delhi a memorable phase of my life. I owe a debt of gratitude to Tapas Tripura, Shailesh Garg, Tushar, Sawan Kumar, Vagish Kumar, and many others for their encouragement and camaraderie. The pang of separation from home was appreciably mitigated by the warmth of friends who became my family during this journeyArshita A., Anagha P, Neethu B., Athira A., Alen, Gayathri, and Sunil, among others.

Last but not least, I owe a profound debt of gratitude to my familymy parents, brother, and wife for their patience, understanding, and unwavering moral support throughout this journey. Their constant encouragement and belief in my abilities provided a firm footing for this accomplishment. Without their sacrifices and steadfast support, this milestone would have been unattainable.

Navaneeth N

Abstract

Practical engineering systems inherently exhibit uncertainties arising from factors such as random variations in geometry, material properties, boundary conditions, and loading scenarios. Despite these uncertainties, ensuring that systems consistently meet desired performance standards during operation remains a critical requirement. Consequently, the quantitative assessment of these uncertainties is indispensable, necessitating their systematic incorporation into analysis and design frameworks. Achieving this demands robust methodologies that integrate probability, statistics, and the principles of mathematical and physical sciences for uncertainty quantification and reliability analysis. However, such frameworks often encounter computational bottlenecks, particularly due to the reliance on expensive numerical solvers. On the other hand, analytical approximation methods may yield unreliable solutions or fail to handle irregular domains and high-dimensional input spaces effectively.

Traditional surrogate-based approaches offer partial relief from these challenges but are not without their own limitations. They often struggle with high input dimensionality, require extensive training data, exhibit limited generalizability beyond the training domain, and face difficulties in addressing long-term, time-dependent problems. These shortcomings underscore the need for innovative modeling methodologies that are computationally efficient and scalable. This thesis addresses these gaps by developing a suite of advanced machine-learning methods tailored to solve stochastic mechanics problems under parametric uncertainty, providing a foundation for accurate, reliable, and scalable uncertainty quantification in complex engineering systems

Dealing with high dimensional inputs is one of the persisting problems in uncertainty quantification and reliability analysis. Traditional approaches often rely on dimensionality reduction techniques to identify a low-dimensional manifold, enabling surrogate models to be trained in this reduced space. Unsupervised dimensionality reduction methods, such as Principal Component Analysis (PCA), are widely used to approximate lower-dimensional representations based solely on input variable information. However, these methods disregard the target data (i.e., the quantity of interest) and often fail to effectively reduce dimensionality, particularly when all input variables contribute nearly equally to the output. To overcome these limitations, this thesis proposes a novel approach for solving high-dimensional reliability analysis problems. The proposed method employs the active sub-

space algorithm to learn a low-dimensional manifold by leveraging the gradient information of the response variable. Recognizing the challenges in gradient estimation, the framework integrates a sparse learning algorithm with the active subspace method, resulting in the Sparse Active Subspace (SAS) algorithm. This approach projects high-dimensional inputs onto a reduced-dimensional space identified by SAS, where a more accurate surrogate model, the Hybrid Polynomial Correlated Function Expansion (HPCFE), maps the inputs to the output response. The resulting framework proves highly efficient for time-independent reliability analysis in high-dimensional systems. However, direct application to dynamic systems remains a limitation, necessitating further advancements.

Modeling the reliability of complex and nonlinear dynamical systems remains a significant challenge in structural reliability and uncertainty quantification, as most traditional methods are constrained to time-independent systems. To address this limitation, this thesis introduces a Koopman operator-based approach for time-dependent reliability analysis. Koopman theory enables the transformation of nonlinear dynamical systems into linear ones by identifying intrinsic coordinates, allowing the seamless computation of time evolution even for systems exhibiting nonlinear or chaotic behavior. However, determining these intrinsic coordinates has traditionally been a challenging task.

To overcome this, a novel deep learning framework is developed that learns Koopman observables in an end-to-end manner, subsequently using these observables for time marching the systems dynamic response. Two distinct architectures are proposed: one tailored for systems with uncertainties in initial conditions and the other designed for systems with uncertainties in underlying parameters. These frameworks demonstrate robustness and the ability to generalize to unseen environments, effectively handling out-of-distribution predictions. However, despite its strengths, the direct application of the Koopman-based approach to long-term response prediction does not yield satisfactory results. This necessitates extending the frameworks capabilities to address such scenarios. To this end, a novel operator learning approach, referred to as the “Waveformer”, is proposed to model dynamical systems with enhanced accuracy and scalability. The Waveformer integrates wavelet transforms for capturing the spatial multi-scale behavior of the solution field with transformers for modeling long-horizon temporal dynamics. Numerical evaluations highlight the Waveformers exceptional performance in learning solution operators, significantly surpassing existing state-of-the-art operator learning methods, particularly in extrapolation tasks. Furthermore, waveformer performs exceedingly well in solving uncertainty quantification and time-dependent reliability analysis problems. This advancement paves the way for more reliable and efficient modeling of dynamical systems under uncertainty.

While the developed frameworks demonstrate strong performance in uncertainty quantification for high-dimensional systems, they are notably data-intensive, relying on extensive training datasets that are typically generated using computationally expensive solvers. This reliance poses a significant challenge for scaling these methods to more complex systems. To address this, Physics-Informed Neural Networks (PINNs) have emerged as a promising alternative. By embedding governing physical laws directly into the training process, PINNs reduce the dependency on labeled data. However, standard PINNs encounter limitations when applied to problems with complex solution domains or discontinuities, as the reliance on automatic differentiation creates a computational bottleneck and impacts performance. To overcome this limitation, a novel Stochastic Projection-based Gradient-Free Physics-Informed Neural Network (SP-PINN) is proposed. This framework combines the

stochastic projection theory with the principles of PINNs, and is proven to be efficacious in problems involving the regular domain, complex domain, and complex response. Unlike traditional PINNs, SP-PINN avoids the reliance on automatic differentiation, allowing for the incorporation of non-differentiable neural network architectures, such as convolutional neural networks, into the training process. This flexibility makes SP-PINN particularly effective across a range of problems, including those with regular domains, irregular geometries, and intricate solution responses. However, despite its success in achieving high accuracy for fixed input conditions, SP-PINN requires retraining whenever boundary conditions, initial conditions, or source terms change, limiting its applicability to stochastic mechanics problems. To address this limitation, a physics-informed wavelet neural operator (PIWNO) is proposed in this thesis that can seamlessly solve both time-dependent and time-independent reliability analysis problems. By integrating physical principles directly into the learning process, PIWNO eliminates the need for labeled training data generated by conventional solvers, offering a robust and efficient framework for solving families of parametric PDEs across a variety of engineering and scientific domains.

The final part of this thesis extends the development of advanced operator learning frameworks to address two critical applications: reliability analysis using the PIWNO and cardiovascular modeling with the geometry-adaptive waveformer. For reliability analysis, PIWNO was employed to tackle high-dimensional engineering systems governed by parametric uncertainties, including diffusion-reaction systems and fluid flow through porous media. Both time-independent and time-dependent reliability analysis problems were tackled. By integrating physical laws directly into the learning process, PIWNO eliminates the dependency on labeled datasets, offering an efficient and scalable solution for quantifying uncertainties and reliability analysis in high-dimensional stochastic systems. For cardiovascular modeling, the waveformer was extended to handle irregular anatomical geometries and the time-dependent dynamics of cardiovascular systems. A geometry-adaptive approach was developed, transforming data from the irregular spatial domain into a regular latent space to efficiently learn patient-specific dynamics. The results obtained are found to be highly accurate, with a coefficient of determination over 0.9 in most cases. These advancements illustrate the potential of the developed frameworks to tackle diverse real-world problems, from engineering reliability to biomedical applications, while addressing computational challenges and enabling scalable, efficient solutions.

सारांश

व्यावहारिक इंजीनियरिंग प्रणालियाँ स्वाभाविक रूप से ज्यामिति में यादृच्छिक भिन्नताओं, भौतिक गुणों, सीमा स्थितियों और लोडिंग सिस्टम जैसे कारकों से उत्पन्न होने वाली अनिश्चितताओं को प्रदर्शित करती हैं। इन अनिश्चितताओं के बावजूद, यह सुनिश्चित करना कि संचालन के दौरान प्रणालियाँ लगातार वांछित उद्देश्य मानकों को पूरा करती हैं, एक महत्वपूर्ण आवश्यकता बनी हुई है। नतीजतन, इन अनिश्चितताओं का गुणात्मक मूल्यांकन अपरिहार्य है, जिससे विश्लेषण और डिजाइन ढांचे में उनके व्यवस्थित समावेश की आवश्यकता होती है। इसे प्राप्त करने के लिए मजबूत विधि की आवश्यकता होती है जो अनिश्चितता परिमाणीकरण और विश्वसनीयता विश्लेषण के लिए संभावना, सांख्यिकी और गणितीय और भौतिक विज्ञान के सिद्धांतों को एकीकृत करती है। हालांकि, इस तरह के ढांचे अक्सर कम्प्यूटेशनल बाधाओं का सामना करते हैं, विशेष रूप से महंगे संख्यात्मक सॉल्वर पर निर्भरता के कारण। दूसरी ओर, विश्लेषणात्मक सन्निकटन विधियाँ अविश्वसनीय समाधान दे सकती हैं या अनियमित डोमेन और उच्च-आयामी इनपुट स्पेस को प्रभावी ढंग से संभालने में विफल हो सकती हैं।

पारंपरिक सरोगेट-आधारित दृष्टिकोण इन चुनौतियों से आंशिक राहत प्रदान करते हैं लेकिन उनकी अपनी सीमाओं के बिना नहीं हैं। वे अक्सर उच्च इनपुट आयाम के साथ संघर्ष करते हैं, व्यापक प्रशिक्षण डेटा की फिर से आवश्यकता होती है, प्रशिक्षण क्षेत्र से परे सीमित सामान्यता प्रदर्शित करते हैं, और दीर्घकालिक, समय-निर्भर समस्याओं को संबोधित करने में कठिनाइयों का सामना करते हैं। ये संक्षिप्त विवरण नवीन मॉडलिंग पद्धतियों की आवश्यकता को रेखांकित करते हैं जो कम्प्यूटेशनल रूप से कुशल और स्केलेबल हों। यह थीसिस जटिल इंजीनियरिंग प्रणालियों में सटीक, विश्वसनीय और स्केलेबल अनिश्चितता के लिए एक आधार प्रदान करते हुए पैमानों की अनिश्चितता के तहत यादृच्छिक यांत्रिकी समस्याओं को हल करने के लिए उन्नत मशीन-लर्निंग विधियों का एक समूह विकसित करके इन अंतरालों को संबोधित करता है।

उच्च आयामी निवेशों से निपटना अनिश्चितता और विश्वसनीयता विश्लेषण की निरंतर समस्याओं में से एक है। पारंपरिक दृष्टिकोण अक्सर कम आयामी मैनिफोल्ड की पहचान करने के लिए आयामी पुनर्वितरण तकनीकों पर निर्भर करते हैं, जिससे सरोगेट मॉडल को इस कम स्थान में प्रशिक्षित किया जा सकता है। प्रिंसिपल कंपोनेंट एनालिसिस (PCA) जैसी गैर-पर्यवेक्षित आयामी कमी विधियों का व्यापक रूप से केवल इनपुट परिवर्तनीय जानकारी के आधार पर निम्न-आयामी प्रतिनिधित्वों का अनुमान लगाने के लिए उपयोग किया जाता है। हालांकि, ये तरीके लक्ष्य डेटा (i.e., ब्याज की मात्रा) का सम्मान नहीं करते हैं और अक्सर आयाम को प्रभावी ढंग से कम करने में विफल रहते हैं, खासकर जब सभी इनपुट चर लगभग समान रूप से योगदान करते हैं। इन सीमाओं को दूर करने के लिए, यह शोध प्रबंध उच्च आयामी विश्वसनीयता विश्लेषण समस्याओं को हल करने के लिए एक नए दृष्टिकोण का प्रस्ताव करता है। प्रस्तावित विधि प्रतिक्रिया चर की ढाल जानकारी का लाभ उठाकर एक निम्न-आयामी मैनिफोल्ड सीखने के लिए ऐक्टिव सबस्पेस (AS) एल्गोरिथ्म को नियोजित करती है। ढाल आकलन में चुनौतियों को पहचानते हुए, फ्रेम-वर्क ऐक्टिव सबस्पेस विधि के साथ एक विरल शिक्षण एल्गोरिदम को एकीकृत करता है, जिसके परिणामस्वरूप स्पार्स ऐक्टिव सबस्पेस (SAS) एल्गोरिदम होता है। यह दृष्टिकोण SAS द्वारा पहचाने गए एक कम-आयामी स्थान पर उच्च-आयामी इन-पुट को प्रोजेक्ट करता है, जहां एक अधिक सटीक सरोगेट मॉडल, हाइब्रिड पॉलीनोमियल कोरिलेटेड फंक्शन एक्सपेंशन (HPCFE) आउटपुट प्रतिक्रिया

के लिए इनपुट को मैप करता है। परिणामी ढांचा उच्च-आयामी प्रणालियों में समय-स्वतंत्र विश्वसनीयता विश्लेषण के लिए अत्यधिक कुशल साबित होता है। हालांकि, गतिशील प्रणालियों के लिए प्रत्यक्ष अनुप्रयोग एक सीमा बनी हुई है, जिससे आगे की प्रगति की आवश्यकता है।

जटिल और अरैखिक गतिशील प्रणालियों की विश्वसनीयता का प्रतिरूपण संरचनात्मक विश्वसनीयता और अनिश्चितता परिमाणीकरण में एक महत्वपूर्ण चुनौती बनी हुई है, क्योंकि अधिकांश पारंपरिक तरीके समय-स्वतंत्र प्रणालियों तक सीमित हैं। इस सीमा को दूर करने के लिए, यह समय-निर्भर विश्वसनीयता विश्लेषण के लिए कूपमैन ऑपरेटर-आधारित दृष्टिकोण पेश करता है। कूपमैन सिद्धांत आंतरिक निर्देशांकों की पहचान करके अरैखिक गतिशील प्रणालियों को रैखिक प्रणालियों में बदलने में सक्षम बनाता है, जिससे अरैखिक या अराजक व्यवहार प्रदर्शित करने वाली प्रणालियों के लिए भी समय के विकास की निर्बाध गणना की अनुमति मिलती है। हालांकि, इन आंतरिक निर्देशांकों का निर्धारण पारंपरिक रूप से एक चुनौतीपूर्ण कार्य रहा है।

इस पर काबू पाने के लिए, एक नया गहन शिक्षण ढांचा विकसित किया गया है जो कूपमैन ऑब्ज़र्वेबल्स को एंड-टू-एंड तरीके से सीखता है, बाद में सिस्टम की गतिशील प्रतिक्रिया को आगे बढ़ाने के लिए इन ऑब्ज़र्वेबल्स का उपयोग करता है। दो अलग-अलग वास्तुकला प्रस्तावित हैं: एक प्रारंभिक स्थितियों में अनिश्चितताओं वाली प्रणालियों के लिए तैयार किया गया है और दूसरा अंतर्निहित मापदंडों में अनिश्चितताओं वाली प्रणालियों के लिए डिज़ाइन किया गया है। ये ढांचे मजबूती और अदृश्य वातावरण में सामान्यीकरण करने की क्षमता को प्रदर्शित करते हैं, प्रभावी रूप से वितरण से बाहर की भविष्यवाणियों को संभालते हैं। हालांकि, इसकी ताकत के बावजूद, दीर्घकालिक प्रतिक्रिया भविष्यवाणी के लिए कूपमैन-आधारित दृष्टिकोण के प्रत्यक्ष अनुप्रयोग से संतोषजनक परिणाम नहीं मिलते हैं। इसके लिए ऐसी स्थितियों से निपटने के लिए ढांचे की क्षमताओं का विस्तार करने की आवश्यकता है। इसके लिए, एक नया प्रचालक अधिगम दृष्टिकोण, जिसे "वेवफॉर्मर" के रूप में संदर्भित किया जाता है, उन्नत सटीकता और मापनीयता के साथ गतिशील प्रणालियों का मॉडल बनाने के लिए प्रस्तावित किया गया है। वेवफॉर्मर लॉन्ग-होराइजन टेम्पोरल डायनामिक्स के मॉडलिंग के लिए ट्रांसफॉर्मर के साथ समाधान क्षेत्र के स्थानिक बहु-स्तरीय व्यवहार को पकड़ने के लिए वेवलेट ट्रांसफॉर्म को एकीकृत करता है। संख्यात्मक मूल्यांकन लर्निंग सॉल्यूशन ऑपरेटर्स में वेवफॉर्मर के असाधारण प्रदर्शन को उजागर करते हैं, विशेष रूप से एकसट्रापोलेशन कार्यों में मौजूदा अत्याधुनिक ऑपरेटर सीखने के तरीकों को महत्वपूर्ण रूप से आगे बढ़ाते हैं। इसके अलावा, वेवफॉर्मर अनिश्चितता की मात्रा और समय-निर्भर विश्वसनीयता विश्लेषण समस्याओं को हल करने में बहुत अच्छा प्रदर्शन करता है। यह प्रगति अनिश्चितता के तहत गतिशील प्रणालियों के अधिक विश्वसनीय और कुशल मॉडलिंग का मार्ग प्रशस्त करती है।

जबकि विकसित ढांचे उच्च-आयामी प्रणालियों के लिए अनिश्चितता मात्रात्मकता में मजबूत प्रदर्शन प्रदर्शित करते हैं, वे विशेष रूप से डेटा-गहन हैं, जो व्यापक प्रशिक्षण डेटासेट पर निर्भर करते हैं जो आमतौर पर कम्प्यूटेशनल रूप से महंगे सॉल्वर का उपयोग करके उत्पन्न होते हैं। यह निर्भरता इन विधियों को अधिक जटिल प्रणालियों तक बढ़ाने के लिए एक महत्वपूर्ण चुनौती पेश करती है। इससे निपटने के लिए फिज़िक्स-इन्फॉर्म्ड न्यूरल नेटवर्क्स (PINNs) एक आशाजनक विकल्प के रूप में उभरे हैं। शासी भौतिक नियमों को सीधे प्रशिक्षण प्रक्रिया में एम्बेड करके, PINNs लेबल किए गए डेटा पर निर्भरता को कम करते हैं। हालांकि, मानक PINNs जटिल समाधान डोमेन या असंतुलन वाली समस्याओं पर लागू होने पर सीमाओं का सामना करते हैं, क्योंकि स्वचालित विभेदन पर निर्भरता एक कम्प्यूटेशनल अड़चन और प्रदर्शन प्रभाव पैदा करती है। इस सीमा को दूर करने के लिए, एक नया स्टोकेस्टिक प्रोजेक्शन-आधारित ग्रेडिएंट-फ्री फिज़िक्स-इन्फॉर्म्ड न्यूरल नेटवर्क (SP-PINN) प्रस्तावित किया गया है। यह ढांचा स्टोकेस्टिक प्रोजेक्शन सिद्धांत को PINNs के सिद्धांतों के साथ जोड़ता है, और नियमित क्षेत्र, जटिल क्षेत्र और जटिल प्रतिक्रिया से जुड़ी समस्याओं में प्रभावी साबित होता है। पारंपरिक (PINNs) के विपरीत, SP-PINN स्वचालित विभेदन पर निर्भरता से बचाता है, जिससे प्रशिक्षण प्रक्रिया में गैर-विभेदक तंत्रिका नेटवर्क वास्तुकला, जैसे कि कन्वोलुशनल न्यूरल नेटवर्क्स (CNNs) को शामिल करने की अनुमति मिलती है। यह लचीलापन SP-PINN को नियमित डोमेन, अनियमित ज्यामिति और जटिल समाधान प्रतिक्रियाओं सहित कई समस्याओं में विशेष रूप से प्रभावी बनाता है। हालांकि, निश्चित इनपुट शर्तों के लिए उच्च सटीकता प्राप्त करने में अपनी सफलता के बावजूद, SP-PINN को जब भी सीमा शर्तों, प्रारंभिक शर्तों, या स्रोत शर्तों में बदलाव होता है तो पुनः प्रशिक्षण की आवश्यकता होती है, जिससे इसकी प्रयोज्यता यादृच्छिक यांत्रिकी समस्याओं तक सीमित हो जाती है। इस सीमा को दूर करने के लिए, इस थीसिस में एक भौतिकी-सूचित वेवलेट न्यूरल ऑपरेटर (PIWNO) का प्रस्ताव किया गया है जो समय-निर्भर और समय-स्वतंत्र विश्वसनीयता विश्लेषण समस्याओं दोनों को निर्बाध रूप से हल कर सकता है। भौतिक सिद्धांतों को सीधे सीखने की प्रक्रिया में एकीकृत करके, PIWNO पारंपरिक समाधानकर्ताओं द्वारा उत्पन्न लेबल किए गए प्रशिक्षण डेटा की आवश्यकता को समाप्त करता है, जो विभिन्न

प्रकार के इंजीनियरिंग और वैज्ञानिक क्षेत्रों में पैरामीट्रिक आंशिक अवकल समीकरणों (PDEs) के परिवारों को हल करने के लिए एक मजबूत और कुशल ढांचा प्रदान करता है।

इस थीसिस का अंतिम भाग दो महत्वपूर्ण अनुप्रयोगों को संबोधित करने के लिए उन्नत ऑपरेटर लर्निंग फ्रेमवर्क के विकास का विस्तार करता है: PIWNO का उपयोग करके विश्वसनीयता विश्लेषण और ज्यामिति-अनुकूली वेवफॉर्मर के साथ कार्डियोवैस्कुलर मॉडलिंग। विश्वसनीयता विश्लेषण के लिए, PIWNO को पैरामीट्रिक अनिश्चितताओं द्वारा नियंत्रित उच्च-आयामी इंजीनियरिंग प्रणालियों से निपटने के लिए नियोजित किया गया था, जिसमें प्रसार-प्रतिक्रिया प्रणाली और झरझरा मीडिया के माध्यम से द्रव प्रवाह शामिल थे। समय-स्वतंत्र और समय-निर्भर विश्वसनीयता विश्लेषण समस्याओं दोनों से निपटा गया। भौतिक नियमों को सीधे सीखने की प्रक्रिया में एकीकृत करके, PIWNO लेबल किए गए डेटासेट पर निर्भरता को समाप्त करता है, जो उच्च-आयामी यादृच्छिक प्रणालियों में अनिश्चितताओं और विश्वसनीयता विश्लेषण की मात्रा निर्धारित करने के लिए एक कुशल और स्केलेबल समाधान प्रदान करता है। कार्डियोवैस्कुलर मॉडलिंग के लिए, वेवफॉर्मर को अनियमित शारीरिक ज्यामिति और कार्डियोवैस्कुलर सिस्टम की समय-निर्भर गतिशीलता को संभालने के लिए विस्तारित किया गया था। एक ज्यामिति-अनुकूली दृष्टिकोण विकसित किया गया था, जो रोगी-विशिष्ट गतिशीलता को कुशलता से सीखने के लिए अनियमित स्थानिक क्षेत्र से डेटा को एक नियमित अव्यक्त स्थान में बदल देता था। अधिकांश मामलों में 0.9 से अधिक निर्धारण के गुणांक के साथ प्राप्त परिणाम अत्यधिक सटीक पाए जाते हैं। ये प्रगति कम्प्यूटेशनल चुनौतियों को संबोधित करते हुए और स्केलेबल, कुशल समाधान को सक्षम करते हुए, इंजीनियरिंग विश्वसनीयता से लेकर जैव चिकित्सा अनुप्रयोगों तक, विविध वास्तविक दुनिया की समस्याओं से निपटने के लिए विकसित ढांचे की क्षमता को दर्शाती हैं।

Contents

Certificate	i
Acknowledgement	iii
Abstract	v
सारांश	ix
Contents	xiii
List of Figures	xix
List of Tables	xxix
Abbreviations	xxxiii
1 Introduction	1
1.1 General	3
1.2 Literature Review	4
1.2.1 Probability space	4
1.2.2 Random variable	4
1.2.3 Hilbert space	4
1.2.4 Uncertainty Quantification and reliability	5
1.2.4.1 Sources of uncertainties	5
1.2.4.2 Limit state function	5
1.2.5 Analytical approximate methods	6
1.2.6 Simulation methods	7
1.2.6.1 Direct Monte Carlo Simulation	7
1.2.6.2 Enhanced simulation methods	8
1.2.7 Surrogate modeling based Methods	8
1.2.7.1 Polynomial Chaos Expansion	9
1.2.7.2 High-Dimensional Model Representation (HDMR)	11
1.2.7.3 Gaussian process regression	12

1.2.8	Deep-learning methods	14
1.2.8.1	Artificial neural network as surrogate models	15
1.2.8.2	Convolutional Neural Network (CNN)	16
1.2.8.3	Recurrent Neural Network (RNN)	17
1.2.8.4	Long Short-Term Memory (LSTM)	18
1.2.8.5	Gated Recurrent Unit (GRU)	18
1.2.8.6	Transformers	19
1.2.8.7	Graph Neural Network (GNN)	20
1.2.9	Unsupervised learning	21
1.2.9.1	Principle Component Analysis	21
1.2.9.2	Auto-encoder Network	22
1.2.10	Time-dependent reliability analysis	23
1.2.10.1	Extreme value method	23
1.2.10.2	Out-crossing rate method	24
1.2.10.3	Single-loop kriging surrogate modeling	25
1.2.10.4	Random process meta modeling	27
1.3	Objectives and scope of the work	27
1.3.1	Objectives	28
1.3.2	Scope of the work	28
1.4	Organization of the Thesis	28
2	Reduced Order modeling for reliability analysis	31
2.1	General	33
2.2	Sparse active subspace assisted surrogate modelling	34
2.2.1	Active subspace	34
2.2.2	Sparse polynomial chaos expansion	36
2.2.3	Hybrid polynomial correlated function expansion	37
2.2.4	SAS-HPCFE	40
2.3	Results and discussion	44
2.3.1	Sobol function	45
2.3.2	A composite beam	50
2.3.3	Twenty five element space truss	54
2.3.4	A multi-storey building subjected to lateral load	57
2.4	Summary	59
3	Operator Learning for modeling dynamical system under uncertainty	61
3.1	General	63
3.2	Koopman Operator for time-dependent reliability analysis	64
3.2.1	Basic mathematical formulations	64
3.2.2	Data driven Koopman representation	65
3.2.3	Results and discussion	68
3.2.3.1	Duffing oscillator	69
3.2.3.2	Lorenz system	78
3.2.3.3	Burger's Equation	83
3.2.3.4	Navier-Stokes Equation	87
3.3	Waveformer for modeling dynamical systems	89
3.3.1	Wavelet transformation	91
3.3.2	Kernel-based neural Operator theory	91

3.3.3	Waveformer	92
3.3.3.1	Note on the complexity of the waveform	94
3.3.4	Training waveform	95
3.3.5	Attention and kernel integration	96
3.3.6	Results and discussion	97
3.3.6.1	Burgers diffusion dynamics	98
3.3.6.2	Kuramoto Sivasinsky Equation	99
3.3.6.3	2-D Allen-Cahn equation	103
3.3.6.4	2D time-dependent NavierStokes equation	106
3.4	Summary	109
4	Physics informed operator learning	113
4.1	General	115
4.2	Stochastic projection based Physics informed neural network	117
4.2.1	Derivative through stochastic projection method	117
4.2.2	Gradient Free Physics informed Neural network	120
4.2.3	Results and discussion	122
4.2.3.1	Heat conduction Problem	122
4.2.3.2	Viscous Burger's Equation	125
4.2.3.3	Poisson's equation	126
4.2.4	Comparison AD-PINN and SP-PINN for problems involving irregular geometry and non-smooth solution	128
4.2.4.1	Non-homogeneous Poisson's equation	130
4.2.4.2	Poisson equation over L-shaped domain	130
4.2.4.3	Poisson's equation over star-shaped domain	133
4.2.4.4	Fourth-order phase-field fracture problem	135
4.3	Physics informed Wavelet Neural Operator	140
4.3.1	Physics informed neural operators	141
4.3.2	Wavelet neural operator	143
4.3.3	Derivatives through stochastic projection	147
4.3.4	Results and discussion	147
4.3.4.1	Burgers' diffusion dynamics	148
4.3.4.2	Non-homogeneous Poisson's equation	150
4.4	Summary	152
5	Application to reliability analysis: Academic validation examples	155
5.1	General	157
5.2	Methodology	157
5.3	Results and discussion	158
5.3.1	Diffusion-reaction system	158
5.3.2	Impulse transmission in nerve	161
5.3.3	Fluid flow through a porous medium	164
5.3.4	Phase transitions in alloys	167
5.4	Summary	171
6	Application to cardiovascular modeling: A large scale example	175
6.1	General	177
6.2	Technical Context	177
6.3	Methodology	178

6.3.1	Graph operator for encoder and decoder	179
6.3.2	Geometry adaptive waveformer	181
6.4	Results and discussion	182
6.5	Summary	196
7	Conclusion	197
7.1	Summary and main contributions	199
7.1.1	Active space assisted surrogate modeling for time-independent reliability analysis of high dimensional systems	199
7.1.2	Koopman operator for time-dependent reliability analysis	200
7.1.3	Waveformer for modeling dynamical systems under uncertainty	201
7.1.4	Stochastic projection-based physics informed neural network	201
7.1.5	Physics-informed wavelet neural operator	202
7.1.6	Application to reliability analysis: Academic validation examples	202
7.1.7	Geometry adaptive waveformer for cardiovascular modeling: An application to large scale biomechanics problem	203
7.2	Open problems for future work	203
7.2.1	Learning non-linear manifold using active subspace	203
7.2.2	Physics informed waveformer	204
7.2.3	Physics informed operator for learning coupled PDEs	205
	References	207
	Appendices	231
A	Analytical approximate methods and Simulation-Based Methods for Reliability Analysis	231
A.1	Analytical approximate methods	233
A.1.1	Earlier methods	233
A.1.2	Taylor's series-based methods for reliability analysis	233
A.1.2.1	Mean value methods	234
A.1.2.2	FORM	234
A.1.2.3	SORM	235
A.2	Improvements to the standard monte-carlo simulations	236
A.2.0.1	Importance sampling	236
A.2.0.2	Stratified sampling	237
A.2.0.3	Directional sampling	238
B	Homotopy Algorithm	241
B.1	General	243
B.2	The Homotopy Algorithm	243
B.2.1	Solution Strategy	244
B.2.2	Minimization of objective function	245
B.3	Closure	246
C	Wavelet Transform: Definitions and Formulations	247
C.1	General	249
C.2	Continuous Wavelet Transform (CWT)	249
C.3	Discrete Wavelet Transform (DWT)	250

C.3.1	Discrete Wavelet Transform	250
C.3.2	Filterbank implementation of DWT	250
C.4	Multi-resolution decomposition	250
C.5	Two-dimensional wavelet transform	251
C.5.1	Expansion of two-Dimensional functions	252
C.5.2	Learning decomposed representation of the signal	252
D	Karhunen–Loève Expansion	253
D.1	General	255
D.2	The KL Expansion	255
D.3	Advantages and Disadvantages of KL Expansion	255
D.3.1	Advantages	255
D.3.2	Disadvantages	255
	List of Publications	257
	Author Biodata	259

List of Figures

1.1	Schematic of fully connected neural network	15
2.1	Flow chart describing step-wise procedure for the proposed approach. The portion marked in blue indicates sparse active subspace. The overall framework is referred to as SAS-HPCFE. Here the number of sample points, N_s and multiplying factor of increment in N_s , γ are chosen based on convergence of the results, ϵ_1 represents the maximum truncation error of optimum polynomial order, ϵ_2 is the maximum allowable prediction error of the framework, and μ is the threshold for active subspace.	42
2.2	Convergence of error in SAS with active subspace estimated via Constantine's classic active subspace (CAS) method [1] for the case of sobol function with $m = 100$ is shown.(a) error in gradients estimated using S-PCE,(b) error in subspaces estimated using S-PCE	46
2.3	Convergence of the prediction error (relative L^2 error norm and relative β error) with increasing training samples for the example Sobol function with $m = 100$	47
2.4	Sensitivity of threshold value μ for the case of sobol function with $m = 100$ is shown. (a) Variation of prediction error with μ , (b) Variation of Number of active subspace with μ	50
2.5	Composite beam considered in Example 2.	51
2.6	Convergence of the prediction error (relative L^2 error norm and relative β error) with increasing training samples for composite beam example	52
2.7	Sensitivity of threshold value μ for the case of composite beam example is shown. (a) Variation of prediction error with μ ,(b) Variation of Number of active subspace with μ	53
2.8	Truss with twenty-five elements considered in Example 3; (a) dimensional details along with node and element numbers, (b) loading details	55
2.9	Six-storey building structure considered in example 4	57
3.1	Schematic representation of the proposed Koopman operator-based architecture for systems with uncertainty in the initial conditions.	66

3.2	Schematic representation of the proposed Koopman operator-based architecture for systems with uncertainty in the parameters.	67
3.3	Architecture of proposed Koopman operator-based framework (a fully connected network) for duffing oscillator example with uncertainty in the initial conditions.	70
3.4	Time evolution of state variable of duffing oscillator predicted for random initial conditions; (a) variation of displacement (y) with time, (b) variation of velocity (\dot{y}) with time	71
3.5	Convergence of prediction error (ϵ) with number of training samples N_s for the duffing oscillator with random initial conditions.	72
3.6	Distribution of the Lyapunov time and the divergence rate for Duffing oscillator with uncertainty in the initial conditions	73
3.7	PDF of first passage failure time (kernel smoothing function: normal, bandwidth = 0.1) obtained by MCS (10000 samples), FNN, LSTM and the proposed framework for the duffing oscillator problem with uncertainties in the initial conditions.	74
3.8	PDF of first passage failure time (kernel smoothing function: normal, bandwidth = 0.1) obtained by MCS (10000 samples) and developed Koopman framework for the case involving uncertainties in the initial conditions.	75
3.9	Architecture of proposed Koopman operator-based framework for duffing oscillator example with uncertainty in the system parameters.	76
3.10	Time evolution of the state variables of duffing oscillator with uncertainty in system parameters; (a) variation of displacement (y) with time, (b) variation of velocity (\dot{y}) with time	76
3.11	PDF of first passage failure time (kernel smoothing function: normal, bandwidth = 0.2) obtained using MCS (10000 samples) and the proposed Koopman operator-based framework for the case of uncertainties in the system parameters.	77
3.12	Architecture of proposed Koopman-based framework for Lorenz system example with uncertainty in the initial conditions.	78
3.13	Convergence of prediction error (ϵ) with number of training samples N_s for the Lorenz system with random initial conditions.	79
3.14	Time-evolution of state variables of Lorenz system with random initial conditions; (a) variation of y_1 with time, (b) variation of y_2 with time, (c) variation of y_3 with time	80
3.15	Distribution of the Lyapunov time and the divergence rate for the Lorenz system with uncertainty in the initial conditions	81
3.16	PDF of first passage failure time (kernel smoothing function: normal, bandwidth = 0.2) obtained using MCS (10000 samples), FNN, LSTM, and proposed Koopman operator-based framework for the Lorenz system with uncertainties in the initial conditions	82
3.17	PDF of first passage failure time (kernel smoothing function: normal, bandwidth = 0.2) obtained using MCS and proposed Koopman operator-based framework for the Lorenz system with uncertainties in initial condition.	83
3.18	Time evolution of state variables of Lorenz system for random system parameters; (a) variation of y_1 with time, (b) variation of y_2 with time, (c) variation of y_3 with time.	84

3.19 PDF of failure time (kernel smoothing function: normal, bandwidth = 0.2) obtained by MCS (10000 samples) and Koopman approach for the case of uncertainties in the system parameters.	85
3.20 Proposed Koopman operator-based framework for Burger's example.	86
3.21 Evolution of velocity field u_1 with time predicted by the Koopman framework, with t representing time instances of the given response.	86
3.22 Evolution of velocity field u_2 with time predicted by the Koopman framework, with t representing time instances of the given response.	87
3.23 PDF of first passage failure time (kernel smoothing function: normal, bandwidth = 0.1) for Burger's equation obtained by MCS (5000 samples) and proposed Koopman operator-based framework. The limit states (thresholds) of velocity fields u_1 and u_2 are (a)[1.75, 0.862] (b) [1.78, 0.862] (c) [1.72, 0.865]	88
3.24 PDF of first passage failure time (kernel smoothing function: normal, bandwidth = 0.2) for Burger's equation obtained by MCS (5000 samples) and proposed Koopman operator-based framework. The limit states (threshold) of velocity fields u_1 and u_2 are [1.35, 0.58]. (a) Result at the 20-th grid point on x_1 axis. (b) Result at the 40 th grid point along x_1 axis	89
3.25 Time evolution of vorticity w for the Navier-Stokes equation obtained using numerical simulation and the proposed Koopman operator-based framework, with t representing time instances of the given response.	89
3.26 PDF of first passage failure time (kernel smoothing function: normal, bandwidth = 0.04) obtained using MCS and the proposed Koopman operator-based approach for the 2-D Navier-Stokes example. (a) The limit-state function is based on maximum over the spatial domain (b) the limit-state function is defined at the grid point 20 along x_1 -axis (c) the limit-state function is defined at the grid point 20 along the x_2 axis	90
3.27 A diagrammatic representation of the waveformer architecture. Firstly, inputs are uplifted by passing through local transformation P . The integral layer consists of two separate branches. In the first branch, wavelet decomposition is performed on the uplifted images and then is passed through a transformer. In the second branch, the inputs are directly fed to the other transformer. An activation is applied in the resultant output obtained by summing the outputs of the two branches. Then, the outputs are downlifted by passing through the transformation Q , which yields the prediction $u(x)$	94
3.28 Variation of prediction error (Relative MSE) with time corresponding to the Waveformer, WNO, and the transformer for the Burgers diffusion dynamics example	100
3.29 Predictions for three different test samples of Burger's equation employing waveformer. (Top to bottom) ground truth solution, waveformer prediction, and the error plot with L_1 error.	101
3.30 Mean and standard deviation of the waveformer's predictions compared to the corresponding ground truth for Burgers' equation example under uncertainty in the initial conditions.	101
3.31 PDF of first passage failure time (kernel smoothing function: normal, bandwidth = 0.1) obtained by MCS and waveformer for 1-D Burger's equation.	102
3.32 Variation of prediction error (Relative MSE) with time-steps corresponding to the Waveformer, WNO, and the transformer for the K-S equation example.	103

3.33	Predictions of two different test samples of K-S equation employing waveformer. (Top to bottom) ground truth solution, waveformer prediction, and the error plot with L_1 error.	103
3.34	Mean and standard deviation of the waveformer's predictions compared to the corresponding ground truth for K-S equation under uncertainty in the initial conditions.	104
3.35	PDF of first passage failure time (kernel smoothing function: normal, bandwidth = 0.8) obtained by MCS and waveformer for K-S equation.	104
3.36	Variation of prediction error (Relative MSE) with time corresponding to Waveformer, WNO, and the transformer for the Allen-Cahn example.	105
3.37	Predictions of a single test sample of 2-D Allen-Cahn equation at 4 different time instances employing waveformer. (Top to bottom) ground truth solution, waveformer prediction, and the error plot with L_1 error.	106
3.38	Mean and standard deviation of the waveformer's predictions compared to the corresponding ground truth for 2-D Allen-Cahn equation under uncertainty in the initial conditions.	106
3.39	PDF of first passage failure time (kernel smoothing function: normal, bandwidth = 0.1) obtained by MCS and waveformer for 2-D Allen-Cahn equation.	107
3.40	Variation of prediction error (Relative MSE) with time corresponding to the Waveformer, WNO, and the transformer for the Navier-Stokes equation example.	108
3.41	Predictions obtained by waveformer for a single test sample of 2-D time-dependent Navier-Stokes equation at 4 different time instances. (Top to bottom) ground truth solution, waveformer prediction, and prediction error.	108
3.42	Mean and standard deviation of the waveformer's predictions compared to the corresponding ground truth for 2-D Navier Stokes equation under uncertainty in the initial conditions.	109
3.43	PDF of first passage failure time (kernel smoothing function: normal, bandwidth = 0.1) obtained by MCS and waveformer for 2-D Navier Stokes equation.	109
4.1	Pictorial perception of stochastic projection method: The red dots represent the configuration point, and the black dots are the neighborhood collocation points	122
4.2	Variation of prediction error with total number of collocation points for for the case of 1-D heat conduction example	124
4.3	Results of the 1-D heat conduction example with 2601 collocation points; (a) Solution predicted by the SP-PINN, (b) Actual results, (c) Absolute error of predicted solution with the actual solution	125
4.4	Results of the 1-D heat conduction example with 4225 collocation points; (a) Solution predicted by the SP-PINN, (b) Actual results, (c) Absolute error of predicted solution with the actual solution	125
4.5	Variation of prediction error with number of neighboring collocation points for the case of 1-D Burger example	126
4.6	Results of the 1-D Burger example with 2601 collocation points; (a) Solution predicted by the SP-PINN, (b) Actual results, (c) Absolute error of predicted solution with the actual solution	127

4.7	Results of the 1-D Burger example with 4225 collocation points; (a) Solution predicted by the SP-PINN, (b) Actual results, (c) Absolute error of predicted solution with the actual solution	127
4.8	Variation of prediction error with total number of collocation points for for the case of 2-D Poisson's equation example	129
4.9	Results of the 2-D Poisson's equation with 2601 collocation points; (a) Solution predicted by the SP-PINN, (b) Actual results, (c) Absolute error of predicted solution with the actual solution	129
4.10	Results of the 2-D Poisson's equation with 4225 collocation points; (a) Solution predicted by the SP-PINN, (b) Actual results, (c) Absolute error of predicted solution with the actual solution	129
4.11	Results of the non-homogeneous Poissons example with non zero source function with 2601 collocation points; (a) Solution predicted by the SP-PINN, (b) AD-PINN, (c) Actual solution	131
4.12	Prediction error of the non-homogeneous Poissons example with non zero source function with 2601 collocation points; (a) The absolute error of SP-PINN. (b) The absolute error of AD-PINN	131
4.13	Results of the non-homogeneous Poissons example with non zero source function with 4225 collocation points; (a) Solution predicted by the SP-PINN, (b) AD-PINN, (c) Actual solution	131
4.14	Prediction error of non-homogeneous Poissons example with non zero source function with 4225 collocation points; (a) The absolute error of SP-PINN. (b) The absolute error of AD-PINN	132
4.15	Results of Poisson equation on L-shaped domain; a) Solution predicted by the SP-PINN, (b) AD-PINN, (c) Actual solution	133
4.16	Prediction error of Poisson equation on L-shaped domain; (a) The absolute error of SP-PINN. (b) The absolute error of AD-PINN	133
4.17	Convergence of the prediction error with respect to the number of collocation points for the Poisson equation on an L-shaped domain. Comparison between AD-PINN and SP-PINN is presented in terms of (a) average absolute error and (b) relative L^2 error.	134
4.18	Poisson equation on L-shaped domain; a) Solution predicted by the SP-PINN, (b) AD-PINN, (c) Actual solution	134
4.19	Poisson equation on L-shaped domain; (a) The absolute error of SP-PINN. (b) The absolute error of AD-PINN	135
4.20	The geometry and boundary conditions for single notched plate specimen. The units of the dimensions are in mm	136
4.21	Variation of Phase field Φ a) crack length 2×10^{-3} , (b) crack length 4×10^{-3} (c) 6×10^{-3}	140
4.22	Evolution of the crack; a) Solution predicted by the SP-PINN, (b) AD-PINN, (c) Actual solution	140

4.23	Physics-informed Wavelet Neural Operator (PIWNO). Motivated by the operator theory in classical functional analysis the WNO architecture aims to learn Green's function of underlying PDEs. In WNO the inputs are first lifted to a high-dimensional latent space, over which certain iterations followed by nonlinear activation are applied. The iterations are represented using wavelet kernel integration blocks. It consists of a kernel integration network that learns the kernel of integration and a linear transformation network that learns the kernel integration constants. For learning the kernel, the latent inputs are localized in space-frequency using wavelets, which is a feature of WNO. The integration outputs and the integral constants are added and finally down-lifted to obtain the solution of underlying PDE. The solutions are constrained to satisfy given PDEs, BC, and IC. For devising the PDE constraint, the spatial derivatives are computed through a stochastic projections-based gradient estimation scheme.	146
4.24	The results for the parametric Burger's equation comprised of given initial conditions, corresponding ground truth solutions, predictions, and error plots illustrated with 4 different unseen sample instances. The PIWNO maps the initial conditions to the corresponding solutions $u(x, t)$ over the domain with a Spatio-temporal resolution of 81×81	149
4.25	The results for the Non-homogeneous Poisson's equation comprised of given source functions, corresponding ground truth solutions, predictions, and error plots illustrated with 4 different unseen sample instances. The physics-informed WNO maps the source term $f(x, y)$ to the corresponding solution $u(x, y)$ over the domain with a spatial resolution of 65×65	151
5.1	The results for the Diffusion-reaction system comprised of source functions, ground truth solutions, predictions, and error plots demonstrated for using 2 different unseen sample instances. The PIWNO effectively maps the initial condition to the corresponding solution $u(x, t)$ over the domain, with a spatiotemporal resolution of 81×81	160
5.2	PDF plots of failure time (kernel smoothing function: Gaussian, bandwidth = 1) obtained by MCS and PIWNO trained with varying number of source functions for the diffusion-reaction system	161
5.3	Prediction results of the diffusion-reaction system for the failure probability (P_f) and the reliability index (β) with unceasing limit state threshold, obtained by PIWNO in comparison with the results of MCS, FORM, SORM and data-driven WNOs (trained with a number of samples, $N_s = 300$ and $N_s = 600$)	162
5.4	Intrinsic dimensionality of the input function obtained for example of nerve impulse transmission, where the 99% of the energy is contained in first 10 eigenvalues.	164
5.5	The results for the nerve impulse transmission example comprised of initial conditions, ground truth solutions, predictions, and error plots demonstrated for using 2 different unseen sample instances. The PIWNO effectively maps the initial condition to the corresponding solution $u(x, t)$ over the domain, with a spatiotemporal resolution of 65×65	164

5.6	PDF plots of failure time (kernel smoothing function: Gaussian, bandwidth = 0.75) obtained by MCS and PIWNO trained with varying number of initial conditions for the nerve impulse transmission example	165
5.7	Prediction results of the example: impulse transmission in nerve for the failure probability (P_f) and the reliability index (β) with unceasing limit state threshold, obtained by PIWNO in comparison with the results of MCS, and data-driven WNOs (trained with a number of samples, $N_s = 300$ and $N_s = 600$)	165
5.8	Intrinsic dimensionality of the input function obtained for the example of flow through a porous medium, where the 99% of the energy is contained in the first 358 eigenvalues.	167
5.9	The results for the example of flow through a porous medium comprised parametric permeability fields, ground truth solutions, predictions, and error plots demonstrated for using 2 different unseen sample instances. The PIWNO effectively maps the permeability fields to the corresponding pressure field $u(x, y)$ over the domain, with a spatial resolution of 64×64	168
5.10	PDF plots of peak pressure values (kernel smoothing function: Gaussian, bandwidth = 1) obtained by MCS and PIWNO trained with varying number of permeability field conditions for the example of flow through a porous medium	168
5.11	Prediction results of the example: fluid flow through a porous medium for the failure probability (P_f) and the reliability index (β) with unceasing limit state threshold, obtained by PIWNO in comparison with the results of MCS, and data-driven WNOs (trained with a number of samples, $N_s = 200$ and $N_s = 400$)	169
5.12	Intrinsic dimensionality of the input function obtained for example of phase transitions in alloys, where the 99% of the energy is contained in the first 232 eigenvalues.	170
5.13	The results for example of phase transitions in alloys comprised of given initial field and corresponding ground truth solutions, predictions, and error plots illustrated with an unseen sample instance at time steps 10 s, 14 s, 18 s and 22 s. The PIWNO receives the spatial field, $u(x, y)$ with a resolution of 65×65 , for the initial 10-time steps and which maps to the corresponding solution $u(x, y)$ for the 13 future time-steps	171
5.14	PDF plots of failure time (kernel smoothing function: Gaussian, bandwidth = 1) obtained by MCS and PIWNO for varying limiting state conditions for example of phase transitions in alloys	172
5.15	Prediction results of the example: phase transitions in alloys for the failure probability (P_f) and the reliability index (β) with unceasing limit state threshold, obtained by PIWNO in comparison with the results of MCS, and data-driven WNOs (trained with a number of samples, $N_s = 300$ and $N_s = 600$)	172
6.1	Schematic representing a patient-specific cardiovascular analysis involving computational modeling, post-processing, inference, and diagnosis	178

6.2	Schematic of the geometry-adaptive waveform, which consists of three components: a geometry encoder, a waveform, and a geometry decoder. The initial input, $a_0(x) = u_{0:k}$, is passed through the geometry encoder, which transforms the input into a regular latent grid. The waveform then operates on this latent space. Finally, the geometry decoder maps the output back to the original space to predict the response at the subsequent time step u_{k+1} .	182
6.3	Predictions results of pressure field measured in $mmHg$ for the dataset 1: (Top to bottom) Geometry adaptive waveform prediction, ground truth response, and L_1 error.	185
6.4	Predictions results of flow rates measured in cm^3/s for the dataset 1: (Top to bottom) Geometry adaptive waveform prediction, ground truth response, and L_1 error.	185
6.5	Scatter plots showing the correlation between the predicted response and the ground truth for dataset 1:(a) Pressure, (b) Flow rate	186
6.6	Mean and standard deviation of the predicted responses of the healthy pulmonary model under uncertainty in the initial conditions.	186
6.7	Response PDF of the pressure and flowrate fields of healthy pulmonary model	187
6.8	Predictions results of pressure field measured in $mmHg$ for the dataset 2: (Top to bottom) Geometry adaptive waveform prediction, ground truth response, and L_1 error.	188
6.9	Predictions results of flow rates measured in cm^3/s for the dataset 2: (Top to bottom) Geometry adaptive waveform prediction, ground truth response, and L_1 error.	188
6.10	Scatter plots showing the correlation between the predicted response and the ground truth for dataset 2:(a) Pressure, (b) Flow rate	189
6.11	Mean and standard deviation of the predicted responses of the aorta model affected by coarctation under uncertainty in the initial conditions.	189
6.12	Response PDF of the pressure and flowrate fields of the aorta model affected by coarctation	190
6.13	Predictions results of pressure field measured in $mmHg$ for the dataset 3: (Top to bottom) Geometry adaptive waveform prediction, ground truth response, and L_1 error.	191
6.14	Predictions results of flow rates measured in cm^3/s for the dataset 2: (Top to bottom) Geometry adaptive waveform prediction, ground truth response, and L_1 error.	191
6.15	Scatter plots showing the correlation between the predicted response and the ground truth for dataset 3:(a) Pressure, (b) Flow rate	192
6.16	Mean and standard deviation of the predicted responses of the healthy aorta model 1 under uncertainty in the initial conditions.	192
6.17	Response PDF of the pressure and flowrate fields of the healthy aorta model	193
6.18	Predictions results of pressure field measured in $mmHg$ for the dataset 4: (Top to bottom) Geometry adaptive waveform prediction, ground truth response, and L_1 error.	193
6.19	Predictions results of flow rates measured in cm^3/s for the dataset 2: (Top to bottom) Geometry adaptive waveform prediction, ground truth response, and L_1 error.	194

6.20	Scatter plots showing the correlation between the predicted response and the ground truth for dataset 4:(a) Pressure, (b) Flow rate	194
6.21	Mean and standard deviation of the predicted responses of the healthy aorta model 2 under uncertainty in the initial conditions.	195
6.22	Response PDF of the pressure and flowrate fields of the healthy aorta model 2	195

List of Tables

1.1	The correspondence of the type of orthogonal polynomial with distribution pattern	10
2.1	Error criteria (ϵ_1 and ϵ_2) and threshold (μ) settings for different benchmark problems. Here, ϵ_1 represents the maximum truncation error corresponding to the optimum polynomial order, computed as the cross-validation L^2 error; ϵ_2 denotes the maximum allowable prediction error of the framework; and μ is the threshold for the active subspace. These values determine the convergence and accuracy the trained SAS-HPCFE	45
2.2	Dimensionality reduction achieved using the sparse active subspace method across all the presented examples. The table lists the original input dimension and the corresponding reduced space dimension (r), demonstrating the efficiency of SAS algorithm.	47
2.3	Probability of failure for the Sobol problem with 10 variables obtained using various methods. β_e indicates the reliability index obtained using MCS. The error metric, $\epsilon = \frac{ \beta_e - \beta }{\beta_e} \times 100$	48
2.4	Probability of failure for the Sobol problem with 40 variables obtained by various methods. β_e indicates the reliability index obtained using MCS. The error metric, $\epsilon = \frac{ \beta_e - \beta }{\beta_e} \times 100$	49
2.5	Probability of failure for the Sobol problem with 100 variables obtained by various methods. β_e indicates the reliability index obtained using MCS. The error metric is calculated as, $\epsilon = \frac{ \beta_e - \beta }{\beta_e} \times 100$	49
2.6	Distribution type and distribution parameters for composite beam in Example 2.	51
2.7	Probability of failure for the Composite beam problem obtained by various methods. β_e indicates the reliability index obtained using MCS. The error metric is computed as $\epsilon = \frac{ \beta_e - \beta }{\beta_e} \times 100$	53
2.8	Failure probability estimates for the Composite Beam problem under a modified failure condition resulting from an increase in the allowable stress threshold S	53
2.9	Distribution type and distribution parameters for truss in Example 3.	56

2.10	Probability of failure for the twenty-five element truss problem obtained by various methods. β_e represents the reliability obtained using MCS. The error metric ϵ is computed as, $\epsilon = \frac{ \beta_e - \beta }{\beta_e} \times 100$	56
2.11	Distribution type and distribution parameters for six-storey building in Example 3.	58
2.12	Probability of failure for six storey building obtained by various methods. β_e represents the reliability obtained using MCS. The error metric, ϵ is computed as, $\epsilon = \frac{ \beta_e - \beta }{\beta_e} \times 100$	59
3.1	Mean RMSE and standard deviation for the Duffing oscillator example computed over multiple random seeds.	70
3.2	RMSE for the Duffing oscillator under varying levels of Gaussian noise in the initial conditions.	70
3.3	Sensitivity of RMSE on the latent dimension (model order) for the Duffing oscillator.	71
3.4	Long-term forecasting error for the Duffing oscillator with uncertainties in the initial conditions	73
3.5	Results of first passage failure probability obtained using the developed framework for the case of a duffing oscillator with random initial conditions. The error metric, ϵ is computed as, $\epsilon = \frac{ \beta_e - \beta }{\beta_e} \times 100$, β_e indicates the reliability index obtained using MCS.	74
3.6	Results of first passage failure probability obtained using the developed framework for the case of duffing oscillator with random system parameters. The error metric ϵ is calculated as, $\epsilon = \frac{ \beta_e - \beta }{\beta_e} \times 100$, where β_e indicates the reliability index obtained using MCS.	77
3.7	Mean RMSE and standard deviation for the Lorenz system computed across multiple random seeds.	79
3.8	RMSE for the Lorenz system under varying levels of Gaussian noise in the initial conditions.	80
3.9	Sensitivity of RMSE on the latent dimension (model order) for Lorenz system.	80
3.10	Long-term forecasting error for the Lorenz system with uncertainties in the initial conditions	81
3.11	Results of first passage failure probability obtained using Koopman approach for the case of Lorenz system with random initial conditions. The error metric ϵ is calculated as $\epsilon = \frac{ \beta_e - \beta }{\beta_e} \times 100$, where β_e indicates the reliability index obtained using MCS.	82
3.12	Results of first passage failure probability obtained using Koopman approach for the case of random system parameters. The error metric, ϵ is calculated as, $\epsilon = \frac{ \beta_e - \beta }{\beta_e} \times 100$, where β_e indicates the reliability index obtained using MCS.	84
3.13	Training setup for all benchmark examples.	98
3.14	Architecture specifications of waveformer, WNO, and transformer	98
3.15	Results of the prediction error of the waveformer in comparison with the state-of-the-art operator learning methods	100
3.16	Prediction error corresponding to waveformer, WNO, and transformer for the Burger diffusion dynamics	100
3.17	Prediction error corresponding to waveformer, WNO, and transformer for the Kuramoto Sivasinsky Equation	103

3.18	Prediction error corresponding to waveformer, WNO, and transformer for the Allen-Cahn equation	105
3.19	Prediction error corresponding to the waveformer, WNO, and transformer for the Navier-Stokes equation.	108
3.20	Convergence study for waveformer with change in number of training samples for K-S and Allen-Cahn equations.	109
4.1	Variation of prediction error with the number of neighboring collation points for the case of 1-D heat conduction example	124
4.2	Prediction error with architectures utilising activation functions ELU, Tanh and ReLU for the case of 1-D heat conduction example	124
4.3	Variation of prediction error with number of neighboring collocation points for the case of 1-D Burger example	126
4.4	Prediction error with architectures utilising activation functions ELU, Tanh and ReLU for the case of 1-D Burger example	126
4.5	Variation of prediction error with the number of neighboring collocation points for th case of 2-D Poisson's equation example	128
4.6	Prediction error with architectures utilising activation functions ELU, Tanh and ReLU for the case of 2-D Poisson's equation example	128
4.7	Relative training cost (time) SP-PINN to AD-PINN	130
4.8	Variation of prediction error with number of collocation points for for the case of 2-D Poissons example with non zero source function	132
4.9	Comparison of prediction error for Poisson's example on L-shaped domain . .	132
4.10	Comparison of prediction error for Poisson's example on star-shaped domain	135
4.11	Results of the prediction error of the physics informed WNO for the two illustrated examples. The prediction error corresponds to the relative Mean Square Error (MSE) of the optimized model after training, computed over the test data. N_s represents the number of training samples.	148
4.12	Prediction error statistics across different spatial resolutions	150
4.13	Prediction error statistics across different time horizons	150
5.1	Results of first passage failure probability obtained using proposed framework for the diffusion-reaction system with varying trained source functions.	161
5.2	Effect of grid resolution on probability of failure and reliability index for diffusion-reaction system	161
5.3	Comparison of methods employed to estimate reliability, with a threshold $e_h = 0.85$, based on accuracy and computational cost for diffusion-reaction system	162
5.4	Results of first passage failure probability obtained using the proposed framework for the case of the impulse transmission in nerve example with varying trained initial conditions.	166
5.5	Results of failure probability obtained using proposed framework for the example of flow through a porous medium with varying trained permeability fields.	167
5.6	Results of first passage failure probability obtained using proposed framework for the example of phase transitions in alloys with varying trained initial conditions.	171

6.1	Performance of the geometric adaptive waveformer over datasets of pressure fields corresponding to different artery models.	184
6.2	Performance of the geometric adaptive waveformer over datasets of pressure fields corresponding to different artery models.	184

Abbreviations

FD	Finite Difference
FEM	Finite Element Methods
ODE	Ordinary Differential Equation
PDE	Partial Differential Equation
PCE	Polynomial Chaos Expansion
SAS	Sparse Active Subspace
GP	Gaussian Process
SVM	Support Vector Machine
SVR	Support Vector Regression
PDF	Probability Density Function
FORM	First Order Reliability Method
SORM	Second Order Reliability Method
MCS	Monte Carlo Simulation
HPCFE	Hybrid Polynomial Correlated Function Expansion
ML	Machine Learning
FNN	Fully connected Neural Network
PINN	Physics Informed Neural Network
SP-PINN	Stochastic Projection based Physics Informed Neural Network
GNO	Graph Neural Operator
FNO	Fourier Neural Operator
WNO	Wavelet Neural Operator
PIWNO	Physics Informed Wavelet Neural Operator
ROM	Reduced Order Modelling